International Journal of Thin Films Science and Technology

http://dx.doi.org/10.18576/ijtfst/050201

Modeling Bipolar Charge Transport in Layered Polymer Films with Graded Permittivity Layers

Meng H. Lean[*] *and Wei-Ping L. Chu*

QEDone LLC, Santa Clara, CA 95054 USA.

Received: 21 Dec. 2015, Revised: 22 Feb. 2016, Accepted: 24 Feb. 2016.
Published online: 1 May 2016.

Abstract: This paper describes the charge transport simulation of graded permittivity layers to enhance the performance and reliability of layered polymer film capacitors for high density energy storage. High **E** field contrast at interfaces is identified as a failure mechanism and field-tailoring is used to develop design guidelines to select optimal graded permittivities. A robust and rapid hybrid boundary integral equation method - Runge-Kutta 4th order total variation diminishing scheme (BIEM-RK4) is used to simulate the proposed design for quantitative comparison. The BIEM-RK4 comprehensively combines the drift-diffusion model with Schottky/Fowler-Nordheim charge injection, Poole-Frenkel field-dependent mobility transport, trapping/de-trapping, and Shockley-Read-Hall recombination for dynamic charge mapping. Results show the significant impact of 32 layers of graded permittivity PMMA tie-layers inserted into a composite 65-layer PC-PMMA-PVDF-PMMA-PC…PC tiered structure where interface field contrast is reduced by 53%; peak field is reduced by 36%; and the corresponding injected leakage current density is reduced by 2x. Results for the original 33-layer PVDF-PC-PVDF…PVDF sample show that the higher dielectric constant (PVDF) material should be used for the outer layer to reduce surface treeing. Additionally, the use of PVDF to contact electrodes severely limits injected currents, mitigating ensuing problems with leakage conduction leading to trapping, field modification, and residual charge issues.

Keywords: Layered polymer film, graded permittivity layer, bipolar charge transport, charge mapping

1 Introduction

Metalized bi-axially oriented polypropylene (BOPP) dielectric thin film capacitors with self-clearing and current carrying capabilities are used in power electronic circuits to enable efficient power conditioning, energy storage, energy conversion, and to provide pulsed power for propulsion, protection, and directed energy systems. Microlayer co-extrusion of two polymers with complimentary properties: polycarbonate (PC) with high breakdown strength; and polyvinylidene fluoride-co-hexafluoropropylene (PVDF-HFP) with high dielectric constant, have resulted in layered films that exhibit enhanced breakdown strength relative to single-layer controls and higher effective dielectric constant based on the compositional percentage of PVDF-HFP to PC [1].

Failure sites from breakdown tests show holes surrounded by treeing patterns in the lateral or in-plane direction compared to the cleaner holes common to single-layer control samples. In layered films subject to divergent needle-plane fields, breakdown characteristics depend on: (1) polarity of the needle with respect to the back plane with a positive needle resulting in more physical damage; and (2) the material that contacts the needle with PC being less penetrating due to higher breakdown strength and lower sub-layer electric (**E**) fields. Effective permittivity, breakdown strength, and energy density measurements indicate improvements with the appropriate PC/PVDF-HFP compositions [2]. Images of treeing structures and punch-through pin holes obtained using focus ion beam (FIB) milling and scanning electron microscopy (SEM) clearly show the extent and nature of damage including delamination, punch-through, voids, and treeing structures [3]. Breakdown in layered structures are influenced by bipolar leakage charge injected from both electrodes which migrate and accumulate at interfaces leading to electric field modification. Interfacial accumulation of charge generated from ionization of impurity sites have been inferred from low field dielectric spectroscopy and matched to diffusion models to extract ion density and diffusion coefficients under thermal equilibrium [4].

Breakdown in layered films is highly dependent on the dynamics of the charge distributions. The presence of a large contrast in permittivity between two material layers gives rise to a highly inhomogeneous electric field and thus significantly reduced effective breakdown strength [5]. This high field contrast at interfaces between low and high permittivity materials is a known issue because most breakdowns have been observed to originate at the layer

[*]Corresponding author E-mail: mhlean@ieee.org

interfaces and emanate from within the middle of the multi-layered film. This paper proposes a fix in the use of graded permittivity layers (GPL) inserted between the PC and PVDF layers to reduce the field contrast by field-tailoring. The material for the GPL is chosen to have permittivity intermediate between PC and PVDF, e.g. Poly(methyl methacrylate) (PMMA) as shown in Figure 1. Bipolar charge transport is simulated to quantify the effect of the GPL. In cases of low diffusion, the method of characteristics (MOC) [6] has been used to derive steady-state solutions for the charge distributions [7].

The modeling of bipolar charge transport in low density polyethylene (LDPE) based on the drift-diffusion equations have employed the finite element method (FEM) in conjunction with Runge-Kutta integration [8]. Similar 1D methods assuming constant mobility without de-trapping have also been reported [9, 10]. More recently, a robust and rapid hybrid time-dependent algorithm was used to calculate dynamic charge maps [11]. Axisymmetric versions of the hybrid algorithm were used to model the divergent field configurations of needle-plane geometries and successfully computed the effects of gaseous voids [12] and predicted the conditions for formation of charge packets [13].

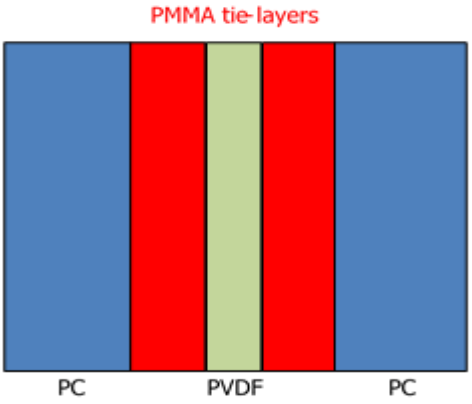

Figure 1: Graded permittivity film cross-section showing PMMA tie-layers inserted between PC and PVDF layers to reduce **E** field contrast.

This comprehensive, self-consistent, simulation method is described for the solution of the drift-diffusion equations for bipolar leakage charge transport through layered polymer thin films. More details and multi-dimensional implementations are available in the literature [11, 12, 13]. This model incorporates current injection via Schottky emission and Fowler-Nordheim tunneling, charge migration via Poole-Frenkel field-dependent mobility, bulk and interfacial charge trapping and de-trapping, and trap-assisted Shockley-Read-Hall species recombination. Current continuity and the rate equations for trapping, de-trapping, and recombination are integrated using a 4th order total variation diminishing Runge-Kutta (TVD-RK4) method with upwind differencing. Charge conservation is handled with a source distribution technique (SDT) to solve the inhomogeneous Poisson equation using the boundary integral equation method (BIEM) based on the free space Green function where conducting and insulating boundaries and material interfaces are represented by equivalent free and bound charge distributions that collectively satisfy all local and far-field boundary conditions. Fields and potentials are defined by superposing integral contributions from all these source types and their distributions. The SDT is uniquely suited for dynamic charge mapping because of the use of physically intuitive charge species. Results for 33-layer PC-PVDF-PC…PC and 65-layer PC-PMMA-PVDF-PMMA-PC…PC configurations are compared and discussed to show the enhanced design and the versatility of this algorithm to handle large numbers of different layered materials.

2 Charge Injection and Transport

2.1 Charge Injection

At moderate applied fields, charge injection from a metal electrode into the lowest unoccupied molecular orbital (LUMO) band of the polymer by Schottky barrier thermionic emission is given by:

$$J_n = AT^2 e^{-\frac{(W_n-\Delta w)}{k_B T/q}} \qquad (1)$$

$$J_p = AT^2 e^{-\frac{(W_p-\Delta w)}{k_B T/q}}$$

where A is the Richardson constant (=1.2×10^6 A/m^2.K^2), and W_n and W_p are the energy barriers to injection in eV. The combined effect of the image force and the applied field results in a lowering of the barrier potential given by:

$$\Delta w = \sqrt{\frac{qE}{4\pi\varepsilon}} \qquad (2)$$

At higher applied fields, the slope gets steeper and the barrier is further lowered so that the tunneling length is much shorter, increasing the probability for tunneling through the barrier. Charge injection from a metal electrode into the polymer is treated using the Fowler-Nordheim quantum mechanical tunneling model given by:

$$J = CE^2 e^{-\frac{\beta}{E}} \qquad (3)$$

where $C = (q^3/16\pi^2 h\Phi_e)$, $\beta = (4\sqrt{2m_e}/3hq)\Phi_e^{3/2}$, m_e is the electron effective mass, h is Planck's constant (4.1356×10^{-15} eV.s), and Φ_e is the effective potential barrier. Φ_e is equal to qW_p or qW_n for positive and negative charge, respectively.

2.2 Field-dependent Mobility

At low-fields and low densities, carriers are almost in equilibrium with the lattice vibrations so the low-field mobility is mainly affected by phonon and Coulomb scattering. The mobility increases until the velocity approaches the random thermal velocity. In a moderately

large electric field, less thermal fluctuation is required to free charge allowing for higher conduction via the Poole-Frenkel mobility:

$$\mu = \mu_0 e^{\gamma\sqrt{E}} \approx \mu_0 e^{\left(\frac{\Delta w}{k_B T/q}\right)} \quad (4)$$

where γ is a constant, and Δw is as defined in (2). At higher electric fields, mobility decreases with increasing electric field due to increased lattice scattering at higher carrier energies, and the carrier velocity saturates. The field-dependent mobility:

$$\mu = \frac{\mu_0}{\left[1+\left(\frac{\mu_0 E}{v_{sat}}\right)^{\beta}\right]^{1/\beta}} \quad (5)$$

enables a smooth transition between low-field and high field behavior where μ_o is the low field mobility at a field of E_o, v_{sat} is the saturation velocity, and β=1 is commonly used [14].

2.3 Charge Attachment/Detachment

Trapping and de-trapping of space charge in polymeric materials are related to the microstructure and morphology of the materials. Charge trapping takes place at a hopping site that requires energy substantially greater than the average energy to release charge carriers. Trapping mechanisms include: physical defects such as dangling bonds which lead to shallow traps; "self" traps due to field modification which alters the length of the polymer chain and their potential well; and chemical defects or impurities which result in deep traps. De-trapping mechanisms may be: photon-assisted by illumination; phonon-assisted through lattice vibration; impact ionization; and tunneling, with the latter two occurring at high fields.

Bulk trapping and de-trapping of bipolar mobile charge may be represented by:

$$\frac{\partial \rho_t^+}{\partial t} = k_t^+ \rho^+ \left(1 - \frac{\rho_t^+}{\rho_\infty}\right) - k_d^+ \rho_t^+ \quad (6)$$

$$\frac{\partial \rho_t^-}{\partial t} = k_t^- \rho^- \left(1 - \frac{\rho_t^-}{\rho_\infty}\right) - k_d^- \rho_t^-$$

where the first and second terms on the right, respectively, denote trapping and de-trapping. The density of trapping states is given by ρ_∞, and k_t is the trapping rate:

$$k_t = \frac{J(t)\sigma}{q} \quad (7)$$

With σ being the trapping cross-section. The de-trapping rate is given by:

$$k_d = N_c \, \nu_{th} \, \sigma \, e^{-E_t/k_B T} \quad (8)$$

where N_c is the effective density of states in the LUMO, v_{th} is the thermal velocity, and E_t is the trap depth. The trapping and de-trapping time constants are the inverse of the rate coefficients. Discharge time characteristics show the existence of a long and a short discharge time constant corresponding to the shallow and deep traps [15].

Analogous expressions for interfacial trapping and de-trapping of bipolar mobile charge are given by:

$$\frac{\partial \lambda_t^+}{\partial t} = k_{t\lambda}^+ \int \rho^+ \, dw \left(1 - \frac{\lambda_t^+}{\lambda_\infty}\right) - k_{d\lambda}^+ \lambda_t^+ \quad (9)$$

$$\frac{\partial \lambda_t^-}{\partial t} = k_{t\lambda}^- \int \rho^- \, dw \left(1 - \frac{\lambda_t^-}{\lambda_\infty}\right) - k_{d\lambda}^- \lambda_{t\lambda}^-$$

With λ_∞ as the density of available states, and $\int \rho dw$ as the Gaussian filter to convert between interface and volume charge within 3 standard deviations from the interface. This conversion is represented as:

$$\int_{\pm 3\sigma} \rho(x) f(x) dx = \lambda|_{x=0} \quad (10)$$

where $\int f(x)dx$=1, and λ denotes the net charge on the electrode-polymer interface, and the sum of polarization and trapped interfacial charge at the polymer-polymer interface. Material interfaces serve as trapping sites, especially for mobile negative charge [16, 17]. Physical interfaces constructed of the same material exhibit the same behavior in allowing the passage of positive charge and to a lesser extent, negative charge.

2.4 Recombination

Charge recombination is trap-assisted analogous to the Shockley-Reed-Hall (SRH) model, and involve the four possible combinations of positive and negative mobile and trapped charge. The recombination equations are given as:

$$U_p = S_2 \rho^+ \rho_t^- + S_3 \rho^+ \rho^- \quad (11)$$

$$U_n = S_1 \rho^- \rho_t^+ + S_3 \rho^- \rho^+$$

where S_1, S_2, and S_3 are recombination coefficients for mobile negative charge and trapped positive charge, mobile positive charge and trapped negative charge, and mobile positive and negative charge, respectively.

3 Simulation Algorithm

3.1 Drift-Diffusion Equations

The bipolar charge transport considered here is drift-diffusion, described as a conduction process governed by an effective field-dependent mobility. Charge carriers are injected from the electrodes into the polymer when they overcome a potential barrier. Schottky emission occurs for moderate fields and transitions to Fowler-Nordheim tunneling at high fields. Injected bipolar carriers drift and diffuse through the polymer in field-dependent transport under the applied and local fields, subject to bulk and interfacial trapping/de-trapping and recombination during transit.

The bipolar charge transport algorithm is defined by the drift-diffusion equations, requiring charge conservation and current continuity given by the following sets of equations:

Current Density

$$\mathbf{J}_n = \rho^- \mu_n \mathbf{E} - D_n \nabla \rho^- \quad (12)$$
$$\mathbf{J}_p = \rho^+ \mu_p \mathbf{E} + D_p \nabla \rho^+$$

Current Continuity

$$\frac{\partial \rho^-}{\partial t} = \nabla \bullet \mathbf{J}_n + U_n \quad (13)$$
$$\frac{\partial \rho^+}{\partial t} = -\nabla \bullet \mathbf{J}_p + U_p$$

Poisson equation

$$\nabla \bullet (\varepsilon \nabla \phi) = -(\rho^+ + \rho^- + \rho_i) \quad (14)$$

where U_n and U_p are the recombination rates, ρ^+ and ρ^- are the positive and mobile negative charge densities, μ_p and μ_n are the positive and negative charge mobilities, D_p and D_n are the positive and negative charge diffusion coefficients, ρ_i is the intrinsic impurity charge density, ε ($=\varepsilon_o\varepsilon_r$) is the permittivity, and the other notations have the usual meanings. The mobility and diffusion coefficients are given by the Einstein relations at equilibrium:

$$\frac{D_n}{\mu_n} = \frac{k_B T}{q} = \frac{D_p}{\mu_p} \quad (15)$$

with k_B ($=1.38065\text{x}10^{-23}$ m^2kg/s^2K) as the Boltzmann constant, T the absolute temperature, and q the Coulomb charge.

This set of equations is similar to those used in conventional semiconductor device modeling where a suitable choice of variables include the natural set: ϕ, *p*, and *n* where the latter two are respectively the positive and negative charge number densities. Solution is derived using a Gummel-like method [18] where the drift-diffusion equations are decoupled and solved sequentially.

3.2 Poisson Solution with the BIEM

The solution of the Poisson equation is obtained using an integral equation method derived from the integral form of the divergence theorem. The BIEM field solver is based on the SDT where the original inhomogeneous domain with mobile, bulk-trapped, and interface-trapped charges together with geometrical boundaries and material interfaces are replaced with an equivalent problem comprised of appropriate distributions of free, bound, and interfacial polarization and trapped charges in free space to satisfy the specified boundary and interface conditions. Once the charge distributions are ascertained, field parameters are evaluated by superposition of the integral contributions from all sources. A Green function method is used where G, the free space Green function, is the fundamental solution to a point charge, or Dirac delta, δ:

$$\nabla^2 G = -\delta(r - r') \quad (16)$$

The solution to the Poisson equation given by

$$\nabla^2 \phi = -\rho/\varepsilon \quad (17)$$

The 1D free space Green function is given by:

$$G[x|x'] = \begin{cases} \frac{(b-x)(x-a)}{(b-a)}; (a \le x < x') \\ \frac{(x'-a)(b-x)}{(b-a)}; (x' < x \le b) \end{cases} \quad (18)$$

where $x \in [a, b]$ denotes the observer, *a* and *b* are the edges of the layer, and x' is the source location or distribution. The **E** field is related to the potential by:

$$\mathbf{E} = -\nabla\phi \quad (19)$$

With potential, ϕ, given by:

$$\phi(x) = \frac{(b-x)}{(b-a)} \int_a^x (x'-a) f(x') dx' + \frac{(b-x)}{(b-a)} \phi(a) + \frac{(x-a)}{(b-a)} \int_x^b (b-x') f(x') dx' + \frac{(x-a)}{(b-a)} \phi(b) \quad (20)$$

where f(x') are the trapped and mobile bipolar charge distributions. The normal derivative is given by:

$$\frac{d\phi(x)}{dx} = -\frac{1}{(b-a)} \int_a^x (x'-a) f(x') dx' - \frac{\phi(a)}{(b-a)} + \frac{1}{(b-a)} \int_x^b (b-x') f(x') dx' + \frac{\phi(b)}{(b-a)} \quad (21)$$

which allow computation of the **E** field within the layer by integration of the analytically differentiable kernels. The integrals in (20) and (21) are evaluated using numerical quadrature by mapping into the two partial integrals, with each integral expressed as the summation of the sampled function with the corresponding weight:

$$\int_a^b F(x)\, dx = \sum_{i=1}^{\infty} w_i f(x_i) \approx \sum_{i=1}^{n} w_i f(x_i) \quad (22)$$

In particular, the Gauss-Jacobi quadrature is a specialized form given by [19]:

$$\int_{-1}^{+1} (1-x)^\alpha (1+x)^\beta f(x)\, dx = \sum_{i=1}^{n} A_i f(x_i) + 0(h)^n \quad (23)$$

Using α=0, β=0, simplifies the integrand to f(x). Sampling locations, x_i, are the *n* roots of the Gauss-Jacobi polynomial, $P_n^{(\alpha,\beta)}(x)$, of degree *n*, and A_i are the coefficients of x_i in $P_n^{(\alpha,\beta)}(x)$ given by:

$$A_i = -\frac{2n+\alpha+\beta+2}{n+a+b+1} \frac{\Gamma(n+a+1)\Gamma(n+b+1)}{(n+a+b+1)(n+1)!} \frac{2^{\alpha+\beta}}{P_n'(x_i) P_{n+1}'(x_i)} \quad (24)$$

Enforcement of boundary conditions for potential and flux and interface conditions at material interfaces for continuity of tangential **E** and normal **D** (intensity):

$$\boldsymbol{n} \times (\boldsymbol{E}_1 - \boldsymbol{E}_2) = 0 \quad (25)$$
$$\mathbf{n} \bullet (\varepsilon_1 \mathbf{E}_1 - \varepsilon_2 \mathbf{E}_2) = \lambda/\varepsilon_o$$

Table 1: Simulation Parameters.

Parameter	Value	Description
μ_p	9 x 10^{-11} $cm^2/V.s$	Mobility of positive charge
μ_n	9 x 10^{-11} $cm^2/V.s$	Mobility of negative charge
D_p	2.33 x10^{-12} cm^2/s	Diffusion coefficient of positive charge
D_n	2.33 x10^{-12} cm^2/s	Diffusion coefficient of negative charge
k^+_{tp}	7 x 10^{-3} /s	Bulk trapping rate for mobile positive charge
k^-_{tp}	7 x 10^{-3} /s	Bulk trapping rate for mobile negative charge
$\rho^+_{t\infty}$	+100 uC/cm^3	Available bulk trapping density for mobile positive charge
$\rho^-_{t\infty}$	−100 uC/cm^3	Available bulk trapping density for mobile negative charge
k^+_{dp}	14 x 10^{-3} /s	Bulk de-trapping rate for trapped positive charge
k^-_{dp}	14 x 10^{-3} /s	Bulk de-trapping rate for trapped negative charge
$k^+_{t\lambda}$	7 x 10^{-3} /s	Interface trapping rate for mobile positive charge
$k^-_{t\lambda}$	7 x 10^{-3} /s	Interface trapping rate for mobile negative charge
$\lambda^+_{t\infty}$	+5 nC/cm^2	Available interface trapping density for mobile positive charge
$\lambda^-_{t\infty}$	−10 nC/cm^2	Available interface trapping density for mobile negative charge
$k^+_{d\lambda}$	14 x 10^{-3} /s	Interface de-trapping rate for trapped positive charge
$k^-_{d\lambda}$	14 x 10^{-3} /s	Interface de-trapping rate for trapped negative charge
S_0	4 x 10^3 $cm^3/C.s$	Trapped negative and trapped positive charge recombination rate
S_1	4 x 10^3 $cm^3/C.s$	Mobile negative and trapped positive charge recombination rate
S_2	4 x 10^3 $cm^3/C.s$	Trapped negative and mobile positive charge recombination rate
S_3	0	Mobile negative and mobile positive charge recombination rate
W_p	1.2 eV	Metal-polymer work function for positive charge
W_n	1.2 eV	Metal-polymer work function for negative charge

result in integral equations for Dirichlet, Neumann, and dielectric interface conditions, respectively, which are then solved simultaneously. These equations incorporate superposition of contributions from sources that include: free charge on electrodes; interface polarization charge; trapped charge on material and physical interfaces, λ; and mobile and trapped volume space charge, ρ. The displacement field, **D**, is related to the **E** field and polarization, **P**, in each layer by the first expression below:

$$\mathbf{D} = \varepsilon_0 \mathbf{E} + \mathbf{P}$$
$$\sigma_{\text{free}} = \mathbf{n}\bullet(\mathbf{D}_2 - \mathbf{D}_1) \quad (26)$$
$$\sigma_{\text{polarization}} = -\mathbf{n}\bullet(\mathbf{P}_2 - \mathbf{P}_1)$$

At the interface between two adjacent polymer layers, the free charge density made up of trapped interfacial space charge, accounts for the jump discontinuity in the normal direction of **D** as shown in the second expression. The corresponding jump discontinuity in the normal direction of **P** gives rise to the polarization charge density shown in the third expression. This latter charge density vanishes for a physical interface between two identical materials. The distributions of free, polarization, and mobile space charge are used in the BIEM to compute the **E** field through the layered polymer sample.

More details on the BIEM are discussed in the literature [20]. The resulting charge map is the taxonomy of the different charge types and their abundance, and presents a dynamic view of the charge kinetics and their temporal and spatial distributions.

3.3 Time Integration Strategy

The current continuity equations together with recombination are integrated using a total variation diminishing (TVD) version of the 4th order Runge-Kutta scheme (TVD-RK4) that guarantees convergence [21]. Spatial differencing uses the upwind scheme which has guaranteed stability [22]. The TVD-RK4 scheme is also used for bulk and interfacial trapping/de-trapping. For example, the 1st order upwind scheme for $\partial u/\partial t + a\partial u/\partial x=0$ is given by:

$$\frac{(u_i^{n+1}-u_i^n)}{\Delta t} + a\frac{(u_i^n-u_{i-1}^n)}{\Delta x} = 0 \text{ for } a > 0 \quad (27)$$
$$\frac{(u_i^{n+1}-u_i^n)}{\Delta t} + a\frac{(u_{i+1}^n-u^n)}{\Delta x} = 0 \text{ for } a < 0$$

where a is the velocity, u is the independent variable, subscript *i* refers to spatial grid index, and superscript *n* refers to iteration time level. The TVD-RK4 advances temporal integration as shown:

$$u^{(1)} = u^n + \Delta t\, L(u^n) \quad (28)$$

with $u^{(1)}$ as the first of the 4th order terms, and du/dt = L(u), where L is an operator [23]. The total variation (TV) is given by:

$$TV = \int \left|\frac{\partial u}{\partial x}\right| dx \approx \sum |u_{i+1} - u_i| \quad (29)$$

integrates the incremental change $|\partial u/\partial x|$ over the entire range of x, and is a property that ensures that $TV(u^{n+1}) \leq TV(u^n)$. The TVD scheme enables sharper shock predictions on coarse grids saving computation time and preventing spurious oscillations in the solution by preserving monotonicity.

The algorithm proceeds through the following steps: (a) bipolar current injection; (b) solve Poisson equation with the BIEM; (c) temporal integration of continuity equation with recombination using TVD-RK4 and upwind scheme; (d) compute changes in bulk and interface trapping/de-

trapping; and (e) update charge arrays and return to step 1. To minimize local error, mesh size, Δh, is required to be smaller than the Debye length, i.e. $L_D = \sqrt{\varepsilon k_B T/q^2 N_i}$, where N_i is the largest charge number density. The time step, Δt, needs to be shorter than the dielectric relaxation time, $\tau=\varepsilon/qN_i\mu$, characteristic of charge fluctuations to decay. The stability criterion of the explicit algorithm is given by the Courant-Friedrichs-Levy (CFL) limit, c:

$$c = \left|\frac{v\Delta t}{\Delta h}\right| \leq 1 \qquad (30)$$

which represents the ratio of mobile charge velocity, ν, to mesh velocity, $\Delta h/\Delta t$. For stability, the mesh velocity cannot be faster than the charge speed [23].

4 Results and Discussion

Bipolar charge transport simulations are performed on 10 μm 33-layer PC-PVDF-PC…PC and PVDF-PC-PVDF…PVDF films, and a 65-layer PC-PMMA-PVDF-PMMA-PC…PC film to generate results to substantiate the enhancement afforded by the use of GPL. The "pull down" test setup uses a parallel capacitor arrangement, allowing simplification to 1D treatment. The setup is biased with a 500 V/s DC ramp until breakdown which occurs at an experimentally determined value of 9675 V or a field of 967.5 V/μm. Simulation parameters used shown in Table 1 are culled from the literature for LDPE [8, 9, 11, 15, 17].

Shown in Figure 2 are the taxonomy of charge types for the 33-layer PC-PVDF-PC…PC film prior to breakdown. Figure 2(a) shows the injected bipolar current densities from t=0 to just before breakdown where the curves follow the exponential dependence on the **E** field of the Schottky emission model. The bipolar mobile charge densities injected, respectively, from the right and the left, are plotted in Figure 2(b) together with their summed result. The bulk trapped charge densities accumulate over time as shown in Figure 2(c) where the dashed lines denote the saturation values prior to breakdown. The trapped interfacial charge densities for the first 4 interfaces encountered by the bipolar charge species are shown in Figure 2(d) where they saturate at the specified values.

PMMA tie-layers are inserted between every PC-PVDF layer to produce the graded permittivity effect using a vol.% loading ratio of 81:10:9 of PC:PMMA:PVDF to result in a 65-layer structure over the 10 μm thick film. The permittivity of the graded layer is chosen to reduce **E** field contrast between two materials with very large difference in dielectric constants, ε_1 and ε_2. To first order, enforcing the equality $\varepsilon_1/\varepsilon_d = \varepsilon_d/\varepsilon_2$ forces the **E** field contrast to be reduced by 50% with $\varepsilon_d = (\varepsilon_1\varepsilon_2)^{1/2}$ where ε_d is the dielectric constant of the graded layer. With permittivities of PVDF and PC at 12 and 3, respectively, the optimal $\varepsilon_d = 6$. Results shown in Figure 3 are for PMMA with a permittivity of 3.9, and should be compared with the corresponding results in Figure 2. In particular, the injected current, mobile charge, and trapped bulk charge densities are all lowered due to the reduced **E** field in each layer caused by insertion of the GPL. Specifically, the injected current is reduced by a factor of 2. The field ratio is reduced to 1.3 and ~3 from 4. Figure 3(d) shows the trapped interface charge for the first 4 interfaces encountered by each polarity of charge where the curves are more compressed in time due to the slower velocities resulting from the lower **E** fields.

Potential profiles through the layered structures are shown in Figure 4 where the 33-layer film exhibits the expected "staircase" ripple effect between alternate layers of different permittivity. The 65-layer film has a smoother profile due to the insertion of the graded permittivity layers. The **E** fields for the 33-layer and 65-layer films are shown superposed in Figure 5 where the global peak is in the middle of the film.

The sequence of events progressing from initial leakage to eventual breakdown requires the field to transform from a Laplacian field (zero space charge) to the "peaked interior" configuration as seen here. Figure 6 shows the zoomed-in view of the center of the multi-layer film extending from one mid-point to the adjacent mid-point of the PC layers showing the **E** field profiles for 33-layer PC-PVDF-PC…PC (blue) and 65-layer PC-PMMA-PVDF-PMMA-PC…PC (brown). The maximum field contrast for the 33-layer film of 1409 V/μm is reduced by insertion of the GPL to 659 V/μm, a reduction of 53%. In addition, the peak field is reduced by 36%.

The departure of the field profile across the film from a Laplacian solution is because of injected bipolar charge from the electrodes. These charges form the mobile space charge and in their migration toward the counter-electrode contribute to the trapped bulk and interfacial charge. The newly injected positive/negative charge raises/lowers the potential adjacent to the anode/cathode, creating the concavity in the potential profile. This effect lowers the field adjacent to the corresponding electrode which raises the field in the interior. Clearly the ensuing trapped bulk and interfacial charge contribute to the progressive increase in the field near the middle of the film.

The preceding results are for layered configurations with PC on the outside. Limiting the amount of injected charge at the electrodes is the key to minimizing the amplitude effects of spatial and temporal charge distributions thus preventing premature breakdown and extending operational life. The one clear way to minimize charge injection is to use the higher dielectric constant material on the outside to contact the electrode. Figure 7 shows results for 33-layer film in PVDF-PC-PVDF…PVDF configuration, i.e. where the electrodes contact the high permittivity PVDF to limit the **E** field. Figure 7(a) shows 10^5x reduction in injected current density compared to Figure 2(a) with Schottky emission. The mobile charge density shown in Figs. 7(b) and 2(b) follow the same trend, i.e. 10^5x reduction in density.

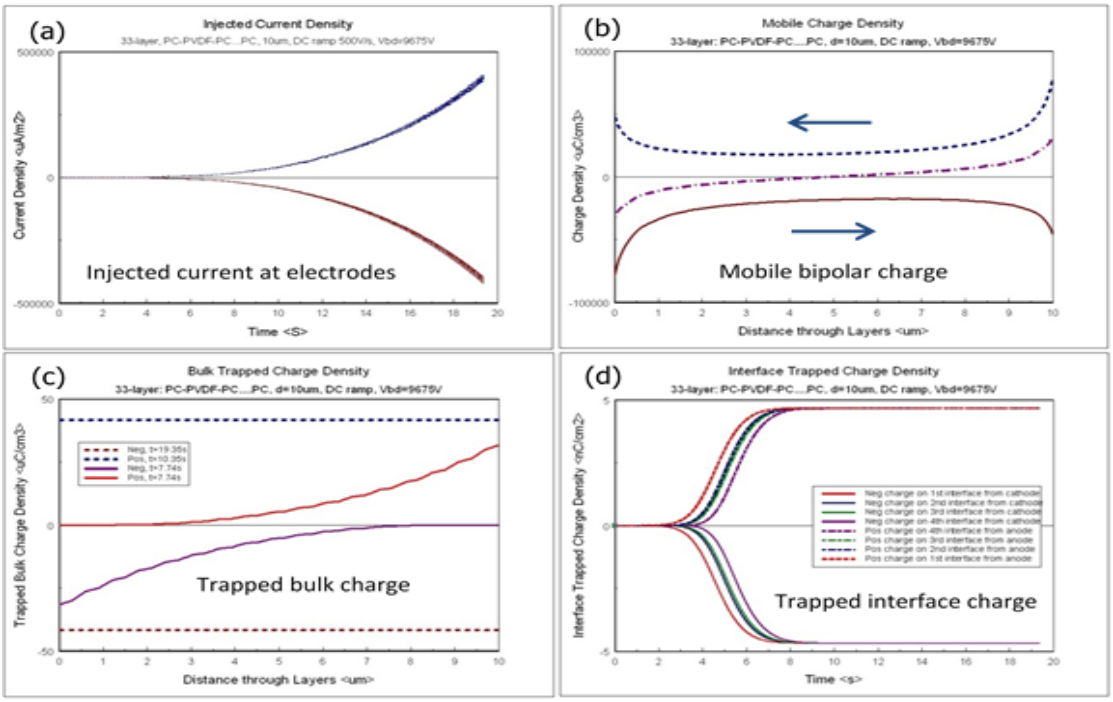

Figure 2: (a) Injected current density; (b) mobile charge density; (c) trapped bulk charge density; and (d) trapped interface charge density for 33-layer PC-PVDF-PC…PC film.

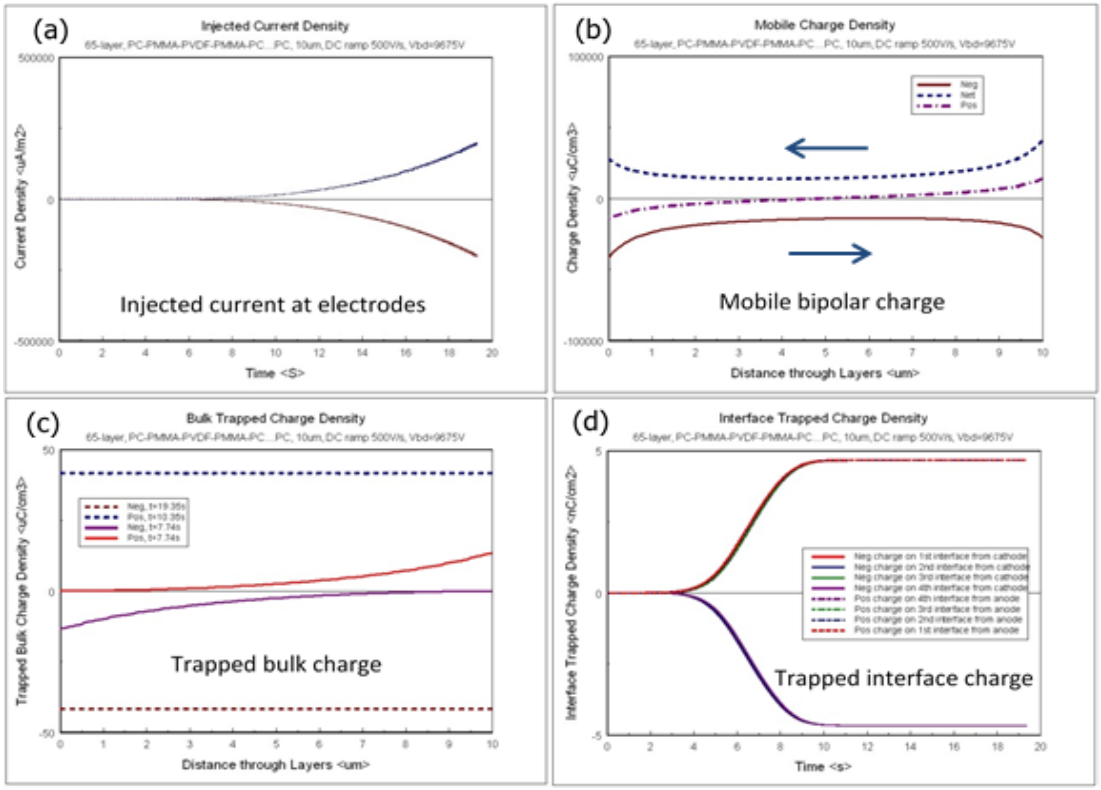

Figure 3: (a) Injected current density; (b) mobile charge density; (c) trapped bulk charge density; and (d) trapped interface charge density for 65-layer PC-PMMA-PVDF-PMMA-PC…PC film.

Figure 8 highlights the **E** field profiles superimposed for the 33-layer PC-PVDF-PC…PC and PVDF-PC-PVDF…PVDF configurations. The much lower injected charge results in very small alteration to the Laplacian field, producing only an insignificant peak field in the center of the film due to reduced leakage charge. This configuration should benefit from GPL insertion as all interfaces may have their field contrasts similarly reduced.

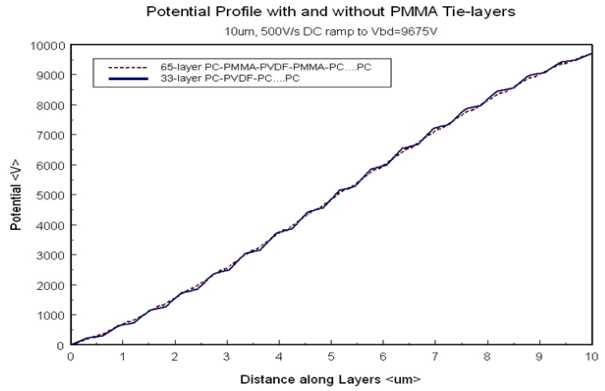

Figure 4: Superposition of potential profiles for 33-layer PC-PVDF-PC…PC and 65-layer PC-PMMA-PVDF-PMMA-PC…PC films showing more conspicuous "staircase" ripple effect of 33-layer structure compared to smoother graded 65-layer structure.

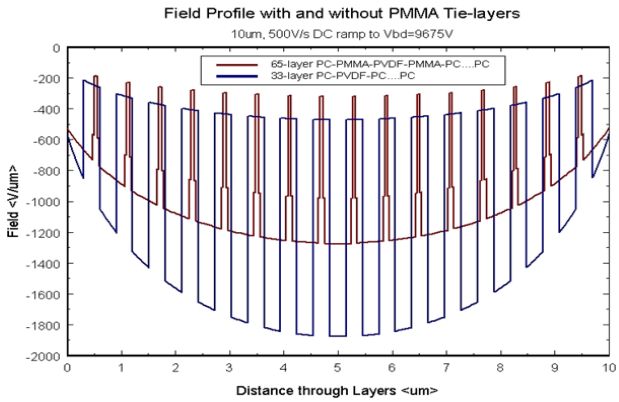

Figure 5: Superposition of layered **E** field profiles for 33-layer PC-PVDF-PC…PC and 65-layer PC-PMMA-PVDF-PMMA-PC…PC films showing interface field contrast reduced by 53%, peak field in PC layer reduced by 36%, and injected current reduced by 2x.

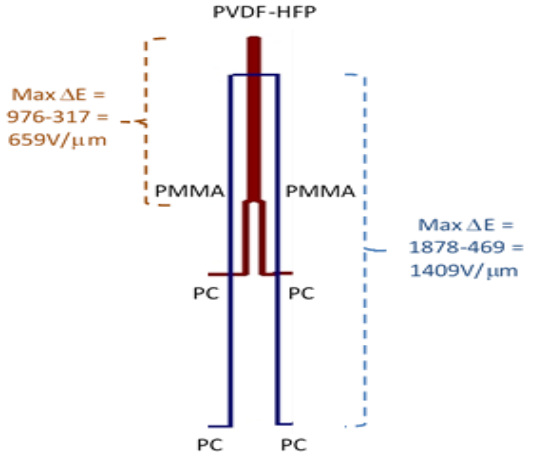

Figure 6: Zoomed-in view of center of multi-layer film from one mid-point to the adjacent mid-point of the PC layers showing the **E** field profiles for 33-layer PC-PVDF-PC…PC (blue) and 65-layer PC-PMMA-PVDF-PMMA-PC…PC (brown).

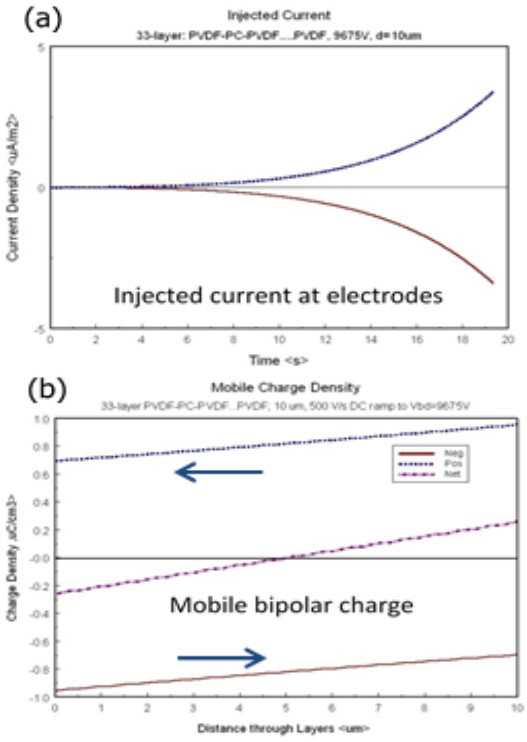

Figure 7: 10 μm 33-layer PVDF-PC-PVDF…PVDF film biased at 9675 V showing high permittivity PVDF in contact with electrodes resulting in 10^5x reduction in: (a) injected current density; and (b) mobile charge density compared to corresponding graphs in Figure 2.

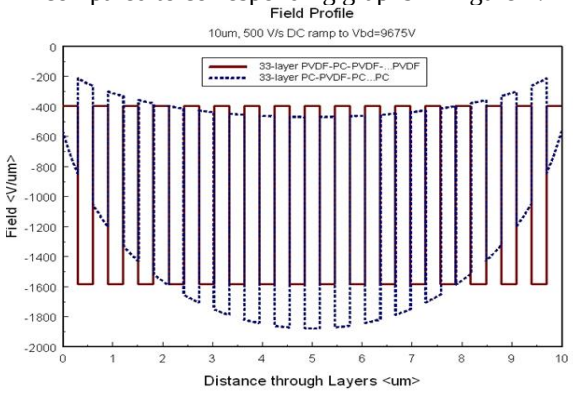

Figure 8: Superposition of layered **E** field profiles for 33-layer PC-PVDF-PC…PC and 33-layer PVDF-PC-PVDF…PVDF films showing both lower **E** field contrast and peak **E** field for the latter case due to the electrode-PVDF contact. Fields are inverted due to flipping of PC and PVDF layers.

5 Conclusions

This paper has described a rapid and robust, self-consistent, comprehensive, hybrid BIEM-RK4 algorithm to simulate the dynamics of bipolar leakage charge injection and transport through multi-layered polymer films including a 33-layer PC-PVDF-PC…PC and improved PMMA tie-layer augmented 65-layer PC-PMMA-PVDF-PMMA-PC…PC and PVDF-PMMA-PC-PMMA-PVDF…PVDF

structures. Simulation results are used to quantitatively compare temporal and spatial charge distributions, and also to compute **E** field contrasts and peaks at interfaces to substantiate the use of GPL to reduce **E** field contrasts and enhance film performance and durability.

The use of PMMA tie-layers with intermediate permittivity between the PC-PVDF materials act to reduce the **E** field contrasts which causes local breakdown and delamination. Alternatively, blend layers of the two materials may also be used to achieve intermediate permittivity with effective permittivity estimated by any of several methods, including the Lichtenecker logarithmic rule and Maxwell-Garnett, Bruggeman, and Loyenga formulae [24]. In addition, the peak **E** field is also reduced together with the level of injected bipolar current. The use of higher dielectric constant materials as the outside layer to contact electrodes result in lower **E** field and consequently lower leakage charge injection. Reducing injected charge limits the secondary effect of bulk and interfacial charge trapping which will lead to further field modification. The use of the PMMA tie-layer with a permittivity of 3.9 improves the design of the layer polymer film and contributes to reduce breakdown probability and longer device life. Further increase up to the theoretical optimum of 6 will result in additional enhancement.

Acknowledgement

Support by the Department of the Navy, Office of Naval Research, grant N000141310064, is gratefully acknowledged.

References

[1] M. Mackey, A. Hiltner, E. Baer, L. Flandin, M.A. Wolakm J.S. Shirk, Enhanced breakdown strength of multilayered films fabricated by forced assembly microlayer coextrusion, J. Phys. D: Appl. Phys., **42**(2009) 175304.

[2] M.A. Wolak, M.J. Pan, A. Wan, J.S. Shirk, M. Mackey, A. Hiltner, E. Baer, L. Flandin, Dielectric response of structured multilayer polymer films fabricated by forced assembly, Appl. Phys. Lett., **92**.(2008) 113301.

[3] M.A. Wolak, A. Wan, J.S. Shirk, M. Mackey, A. Hiltner, E. Baer, Imaging the effect of dielectric breakdown in a multilayered polymer film, J. Appl. Poly. Sci., **123**(2012) 2548-2557.

[4] M. Mackey, D.E. Schuele, L. Zhu, E. Baer, Layer confinement effect on charge migration in polycarbonate/poly(vinylidene fluorid-co-hexafluoropropylene) multilayered films, J. Appl. Phys., **111**(2012) 2548-2557.

[5] Q. Wang, L. Zhu, Polymer nanocomposites for electrical energy storage, J. Poly. Sci. Part B: Poly. Phys., **49**(2011) 1421-1429.

[6] S. Sarra., The Method of Characteristics with applications to Conservation Laws, J. Online Mathematics Appl., **3**(2003).

[7] M.H. Lean, M.A. Wolak, M. Mackey, E. Baer, Simulation of internal field distributions in multilayer Polycarbonate/Poly(vinylidene fluoride) – hexafluoropropylene films at onset of breakdown, IEEE Trans. Diel. Elec. Ins., **21**(2014) 800-808.

[8] I. Boukhris, E. Belgaroui, A. Kallel, Physical and numerical modeling for bipolar charge transport in disordered polyethylene under high DC voltage. Int. J. Elec. Eng. Informatics, **2**(2010) 313-324.

[9] G. Chen, S.H. Loi, Space charge modeling in solid dielectrics under high electric field based on double charge injection model. MRS Fall Meeting (2006).

[10] F. Boufayed, G. Teyssendre, C. Laurent, S. Le Roy, L.A. Dissado, P. Segur, G.C. Montanari, Models of bipolar charge transport in polyethylene, J. Appl. Phys., **100**(2006) 104105.

[11] M.H. Lean, W-P.L. Chu, Dynamic charge mapping in layered polymer films. IEEE Trans. Diel. Elec. Ins., **21**(2014) 1319-1329.

[12] M.H. Lean, W-P.L. Chu, Effect of gaseous void on bipolar charge transport in layered polymer film. J. Phys. D: Appl. Phys., **47**(2014) 075303.

[13] M.H. Lean, W-P.L. Chu, Simulation of charge packet formation in layered polymer film. COMPEL: Int. J. Comp. Math. Elec. & Elec. Eng., **33**(2014) 1396-1415.

[14] D.M. Caughey, R.E. Thomas, Carrier mobilities in silicon empirically related to doping and field, Proc. IEEE, **55**(1967) 2192-2193.

[15] G. Chen, Z. Xu, Charge trapping and de-trapping in polymeric materials, J. Appl. Phys., **106**(2009) 123707-5.

[16] G. Chen, Interfaces and space charge in polymeric insulating materials. U Southampton.

[17] Z. Xu, G. Chen, Interfacial characteristics of space charge in multiplayer LDPE, Proc. Int. Conf. Condition Monitoring and Diagnosis, (2008), Beijing.

[18] R.E. Bank, D.J. Rose, W. Fichtner, Numerical methods for semiconductor device simulation, IEEE Trans. Elec. Dev., **30**(1983) 1031-1041.

[19] A. Abramowitz, I.A. Stegun, In Handbook of Mathematical Functions, Dover Press, New York, (1965) 591-592.

[20] M.H. Lean, Novel integral formulation for scattering from multi-layered dielectric cylinders of arbitrary cross-section, IEEE Trans. Magnetics, **40**(2004) 1476-1479.

[21] F. Kupka, N. Happenhofer, I. Higueras, O. Koch, Total-Variation-Diminishing implicit-explicit Runge-Kutta methods for the simulation of double-diffusive convection in Astrophysics, J. Comp. Phys., **231**(2012) 3561-3586.

[22] E. Fatemi, F. Odeh, Upwind finite difference solutions of Boltzmann equation applied to electron transport in semi-conductor devices, IMA Preprint Series #980 (1992).

[23] S. Gottlieb, C.W. Shu, E. Tadmor, Strong stability-preserving high-order time discretization methods. SIAM Rev., **43**(2001) 89-112.

[24] R. Mekala, N. Badi, Modeling and simulation of high permittivity core-shell ferroelectric polymers for energy storage solutions, Proc. COMSOL Conf., (2013), Boston.